J. Plasma Phys. (2024), *vol*. 90, 905900114 © The Author(s), 2024.
Published by Cambridge University Press
This is an Open Access article, distributed under the terms of the Creative Commons Attribution licence (http://creativecommons.org/licenses/by/4.0/), which permits unrestricted re-use, distribution and reproduction, provided the original article is properly cited.
doi:10.1017/S0022377823001411

Effects of guard and boom on needle Langmuir probes studied with particle-in-cell simulations

S.M. Brask [1,†], **S. Marholm** [1,2], **W.J. Miloch** [1,†] **and R. Marchand** [3,†]

[1]Department of Physics, University of Oslo, PO Box 1048, Blindern, 0316 Oslo, Norway

[2]Department of Computational Materials Processing, Institute for Energy Technology, Instituttveien 18, 2007 Kjeller, Norway

[3]Department of Physics, University of Alberta, Edmonton, AB T6G 2E1, Canada

(Received 7 September 2023; revised 6 December 2023; accepted 7 December 2023)

We investigate the effects of different guard geometries on the currents to needle-type Langmuir probes. The results are based on particle-in-cell numerical simulations. We show that if the guard length is less than 6–8 Debye lengths there can be a significant effect on the currents to the probe. A guard radius should not be larger than the Debye length, otherwise it can also significantly affect the currents. However, since guard radii are often close to the probe radius, the second condition is usually satisfied.

Key words: space plasma physics, plasma simulation, plasma devices

1. Introduction

Current–voltage (I–V) characteristics of electrically conducting surfaces in isotropic plasmas were first discussed by Irvin Langmuir Mott-Smith & Langmuir (1926) with the so-called orbital motion limited (OML) theory. Derivations for ideal planar, spherical and cylindrical electric probes in plasma were done, and such probes are nowadays collectively referred to as Langmuir probes. The Langmuir probe theory was later refined by Laframboise (1966) with such additions as a finite radius of the probe. In space and ionospheric plasma experiments, both spherical and cylindrical probes are commonly used. Langmuir probes have seen a widespread usage both outside the ionosphere, with, e.g., the Rosetta mission, and inside the ionosphere with orbital missions such as Freya, Swarm, Cluster and Norsat-1 (Holback *et al.* 1994; Gustafsson *et al.* 1997; Eriksson *et al.* 2007; Buchert *et al.* 2014; Hoang *et al.* 2018). In addition, Langmuir probes have been deployed in many sub-orbital sounding rocket missions, such as the ICI 1, 2 and 4 rockets or the ECOMA campaign (Bekkeng *et al.* 2010; Jacobsen *et al.* 2010; Bekkeng *et al.* 2013). The Debye length in the ionosphere ranges from a fraction of a millimetre to centimetres, and it is difficult to manufacture such a small spherical probe that will fulfill the OML assumptions and will collect currents with acceptable signal-to-noise levels.

† Email addresses for correspondence:
s.m.brask@fys.uio.no, w.j.miloch@fys.uio.no, rmarchan@ualberta.ca

https://doi.org/10.1017/S0022377823001411 Published online by Cambridge University Press

Thus, cylindrical probes with very small radii are often used. Such small cylindrical probes are often called needle-type probes (Hoang *et al.* 2018).

When a Langmuir probe has a high enough bias voltage, it will collect only charges of a single (opposite) sign. This regime of the probe bias is called saturation. In the ionosphere and space plasma, for a sufficiently high positive bias voltage, only electrons will be collected. Note that if there are different ion species, including negative ions, they will also contribute to the currents in the electron saturation regime. However, in the following we consider probes at a high positive bias, and consider only electrons to be collected in this regime, which is the usual condition in the ionosphere.

For a cylindrical Langmuir probe p in the saturation regime at a voltage V with respect to the background, the collected current due to species α is approximately given by Laframboise (1966)

$$I_{\mathrm{p},\alpha} = I_{\mathrm{th},\alpha} K \left(1 + \frac{q_\alpha V}{k_\mathrm{B} T_\alpha}\right)^{\beta}, \tag{1.1}$$

where $k_\mathrm{B}, q_\alpha, T_\alpha$ are the Boltzmann constant and the charge and temperature of the species, respectively, K is a constant depending on the probe shape with $K = 2/\sqrt{\pi}$ for a cylindrical probe, $I_{\mathrm{th},\alpha} = n_\alpha q S \sqrt{k_\mathrm{B} T_\alpha / 2\pi m_\alpha}$ is the thermal current due to random particle motion through a surface S if the surface and plasma are at the same electric potential and n_α, m_α are the species' number density and mass.

Several assumptions are made in the OML theory for the derivation of (1.1), such as the probe being very long, and the probe radius being very small with respect to the Debye length. Since the β parameter of (1.1) is 1 for a spherical probe, and 0.5 for an infinitely long cylindrical probe, it is assumed that the real effects of both of these assumptions can be captured in the β parameter, with a value approaching 1 as the probe gets shorter (Laframboise 1966; Marholm & Marchand 2020). This was also recently shown to hold true empirically using kinetic numerical simulations by Marholm & Marchand (2020).

Several high-quality corrections have been made to the OML theory recently that are regression based, using nonlinear functions such as radial basis functions (RBFs) or feed-forward neural networks (Olowookere & Marchand 2021; Liu *et al.* 2023). These methods can be used to infer plasma parameters such as temperature or density from simulations using the regression model as a 'black box'. A high degree of complexity can be included, although a complete understanding of the physics is not available. This is possible for specific use cases, for example, by limiting the model to a specific probe geometry, which adds a powerful tool to a specific space mission (Liu *et al.* 2023). In some cases it is also possible to use such methods to construct a more general function, which is more widely applicable (Marholm & Marchand 2020). However, as of now for such general functions, some assumptions need to be made. It is not clear how much these assumptions affect probe measurements. Therefore, in this work we investigate the effect of the two geometrical assumptions commonly made on the guard length and guard radius.

It is quite common in the design of needle Langmuir probes to accept guard lengths as short as 1–2 Debye lengths (Hoang *et al.* 2018). Recent results have shown that the end-effects can reach much longer than one or two shielding lengths, giving some motivation for testing the common 1–2 Debye lengths assumption (Marholm & Marchand 2020). In addition, seldom is the guard radius of particular interest in needle Langmuir probe design, although it is quite reasonable to assume there are some changes in the probe current when a larger current collector is right next to it. To the best of the authors' knowledge, these assumptions have never been tested properly. In this article, we address this issue, so that previous and upcoming probe designs can get substantive information to base their designs upon.

https://doi.org/10.1017/S0022377823001411 Published online by Cambridge University Press

It is useful for the discussion to understand how the model function is derived for the finite-length (FL) theory (see Marholm & Marchand 2020). The Marholm–Marchand model (FL) includes the finite-length end-effects of a cylindrical probe, removing the infinite length probe assumption that was made in the OML theory (Marholm & Marchand 2020). We therefore briefly review it here.

The main idea is that the problem can be described completely by a function that includes all physical parameters that can have an effect. Introducing independent dimensionless variables we can write a relationship between the parameters. The problem can then be reduced by Buckingham's π theorem to yield a function of the form (Buckingham 1914)

$$\mathcal{G}\left(\frac{i}{i_{\mathrm{th}}}, \frac{-qV}{k_{\mathrm{B}}T}, \frac{z}{\lambda_{\mathrm{D}}}, \frac{l}{\lambda_{\mathrm{D}}}, \frac{r}{\lambda_{\mathrm{D}}}, n\lambda_{\mathrm{D}}^3\right) = 0, \tag{1.2}$$

where i/i_{th}, $-qV/k_{\mathrm{B}}T$ are the normalised current and the probe bias potential, z/λ_{D} is the position on the probe, l/λ_{D}, r/λ_{D} are the probe length and radius, respectively, and $n\lambda_{\mathrm{D}}^3$ is the plasma parameter. We use the Debye length λ_{D} to normalise the parameters in length. We omit any subscript for the radius r initially since we consider a single free-floating cylinder. At this point some assumptions are made that reduce the dimensionality of the problem further.

First, it is assumed that the probe is thin $r/\lambda_{\mathrm{D}} \to 0$: this is a usual assumption for the Langmuir probes, and it is often stated as $r/\lambda_{\mathrm{D}} < 1$ (see Laframboise 1966). Second, it is assumed that plasma is weakly coupled i.e. $n\lambda_{\mathrm{D}}^3 \gg 1$, which is also a common assumption. The last two arguments of (1.2) can therefore be disregarded, and the equation can be inverted with respect to the first argument to yield

$$i(z) = i_{\mathrm{th}} g\left(\frac{z}{\lambda_{\mathrm{D}}}; \frac{l}{\lambda_{\mathrm{D}}}, \frac{-qV}{k_{\mathrm{B}}T}\right). \tag{1.3}$$

Equation (1.3) is for the collected current density at position z on the probe, and the total probe current is then the integral of $i(z)$ over the whole surface of the probe. The parameter space, which the simulations need to span is the length of the probe and the probe potential. A Python library using local polynomial regression to make a nonlinear fit of the profile function g was made available by Marholm (2019), and the resulting profile functions and corrected currents are available in the Langmuir library (Marholm & Darian 2021). The g functions in the library were constructed from the simulation made by Marholm & Marchand (2019) as a part of the work by Marholm & Marchand (2020).

Figure 1(*a*) is adopted from Marholm & Marchand (2020), and together with figure 1(*b*), it shows the assumed probe and guard geometry used in this work. In figure 1(*a*) we use the same geometry as Marholm & Marchand (2020), with the addition of a bootstrapped section, also called a spacecraft bus, carrier or boom, on the left side. In this geometry the probe radius and guard radius are the same. In fact, the simulations run in the Marholm–Marchand paper are of a free-floating cylinder, and the guard is imposed by removing a section of the profile function g. It is therefore implicitly assumed that the guard radius has no effect on the probe current. In reality the boom–guard–probe geometry is more complex, and while the removed section of the profile function currently removes one of the end points which typically leads to an increase in the current, a boom will likely lower the current to the same section. In addition, practically the boom–guard–probe system usually needs a guard with a larger radius (Bekkeng *et al.* 2010), which is illustrated in figure 1(*b*), and which likely also affects the currents to the probe. If we where to include one of these additional parameters, for example the guard radius (and even the normalised

https://doi.org/10.1017/S0022377823001411 Published online by Cambridge University Press

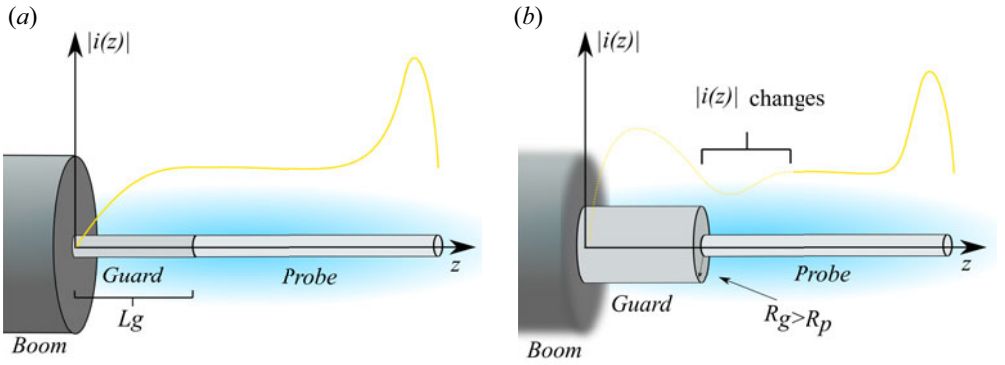

FIGURE 1. Assumed geometry of the needle Langmuir probe and guard in the FL library Marholm & Darian (2021) (*a*) including a carrier (boom), compared with a more realistic geometry (*b*) including a guard with a larger radius R_g. The current $|i(z)|$ curve represents the collected current density on the probe surface as a function of distance z. The dotted part of the $|i(z)|$ curve in (*b*) represents the region where the current density inferred from the FL library is uncertain due to the presence of a guard and boom. In addition, we marked the guard length L_g.

guard length L_g/λ_D), (1.3) must be extended

$$i(z) = i_{OML} g\left(\frac{z}{\lambda_D}; \frac{R_g}{\lambda_D}, \frac{l}{\lambda_D}, \frac{-qV}{k_B T}\right), \tag{1.4}$$

where R_g/λ_D is the normalised guard radius.

It is roughly enough to use 10 data points per dimension to sufficiently describe (1.3) in the range of typical values used in space plasma according to Marholm & Marchand (2020). Therefore, the number of simulations needed to span the two dimensions in (1.3) is $10 \times 10 = 100$. If we were to add one parameter, for example the radius of the guard, and this parameter also needed 10 data points, the total number of simulations needed would increase to $10 \times 10 \times 10 = 1000$. Although this is a large number of simulations, it is not impossible, but for this to be worth the effort, the added parameter should have a significant effect on the probe current.

2. Particle-in-cell simulations

2.1. *Numerical approach*

For all simulations in the present work we use PTetra which is a parallelised 3D particle-in-cell (PIC) simulator (Marchand 2012; Marchand & Resendiz Lira 2017). PTetra is a good choice of simulator to use due to the unstructured grid, giving us a high spatial resolution close to the simulated objects such as probe and guard. In addition, PTetra tracks the current through each surface cell, such that we can get localised currents at discrete points along a simulated surface, and not only the total current to that surface, giving us more information about the current distribution.

2.2. *Simulation set-up*

We have designed numerical experiments so that each simulation has the same inner resolution of $0.056\lambda_D$ and initially use 50×10^6 simulation particles, or so-called super-particles. In every simulation the plasma parameters are $T_e = 0.1$ eV, and $n_e = n_i = 1 \times 10^{11}$ m^{-3}. This gives the Debye length of 7.4 mm. We also set the shortest length

https://doi.org/10.1017/S0022377823001411 Published online by Cambridge University Press

from the simulation outer boundary to any other simulated surface to be $15\lambda_D$. As in the Marholm & Marchand model, plasma is assumed to be stationary. To speed up the simulations a usual technique is to use a modified ion mass, and we use $m_i = 114m_e$. We set a sufficiently high positive bias on the probe and guard, so that the attracted species are the electrons. We also set the probe bias voltage equal to the guard voltage. The currents to the probe do not depend on the ion mass with negligible contributions from the repelled ions, as long as we are in the electron saturation regime, i.e. the probe bias is sufficiently large (Marholm & Marchand 2020). This is the case for all probe bias voltages considered in this study. The simulations are then run for 1×10^{-5} s, or 2.7 ion plasma periods, which is sufficiently long to reach a steady state. To understand the effects of different parts of the Langmuir probe, we split up the geometry and run one set of simulations where we isolate the effects of a charged boom, with varying the guard length L_g. Then we run a second set of simulations where we omit the boom and simulate only the probe and guard, with varying guard radius R_g.

A summary of the parameters for the main set of experiments is listed in table 1. For the first experiment we let L_g vary, and we run the simulations for two probe voltages. In this experiment we use the geometry as in figure 1(*a*) where $R_p = R_g$. In reality, the probe and guard will be attached to some surface. This is typically a boom, which has the same floating potential as the main spacecraft body. Spacecraft charge can be calculated by considering the current contributions of different species (Garrett 1981; Whipple 1981). To calculate some typical values of spacecraft potentials ψ_{sc} in the low Earth orbit (LEO) we can use the equation given by Anderson (2012)

$$\psi_{sc} = -\frac{k_B T_e}{q} \ln \frac{A_e}{A_i} \left[\frac{k_B T_e}{2\pi m_e v_{sc}^2} \right]^{1/2} \tag{2.1}$$

where the fraction of surface accessible to the electrons with respect to ions is given by A_e/A_i, and the spacecraft speed relative to the background plasma is given by v_{sc}. Using typical plasma values, the most realistic values of the spacecraft voltages range from ~ -0.3 V to -0.6 V. It is also noted that spacecraft in LEO rarely experience potentials of more than a few volts negative, which is also supported by observational data (Anderson *et al.* 1994; Anderson 2012). However, there are a few examples of high charging events where potentials can exceed 100 V negative (Gussenhoven *et al.* 1985; Eriksson & Wahlund 2006; Anderson 2012). This is valid for low background plasma density and high flux of precipitating electrons inside the auroral arc. In these cases the electron distributions are likely to be a two-component Maxwellian (Yeh & Gussenhoven 1987). We do not complicate the simulations with adding high-energy precipitating particles at this stage. We therefore use two voltages for the spacecraft/boom in the simulations: we first consider a realistic boom voltage of -0.5 V and, then, a slightly more negative value at -2 V, which are both representative of boom (or spacecraft) voltages in the ionosphere. Due to limited amount of computational resources, we select the most important parameters to vary. Thus, the guard length L_g is varied while the probe length is maintained at $L_p = 10\lambda_D$. We assume that the boom radius is large and set it to $10\lambda_D$. Thus, in this experiment the changes we observe will be attributed to the guard length. We repeat the same process for two different probe radii of $0.1\lambda_D$ and $0.5\lambda_D$, and later refer to these as 'small probe' and 'large probe', and run each configuration for the probe bias voltage of 1 V and 5 V. This gives us 56 simulations in the first numerical experiment.

For the second numerical experiment, we use the geometry as in figure 1(*b*), where the boom is blurred to show that it is removed from the simulations. We remove the

https://doi.org/10.1017/S0022377823001411 Published online by Cambridge University Press

ID	V_p	R_g/R_p	L_g	V_b
$1a : R_p = 0.1\lambda_D$	[1,5] V	1	[1,2,3,4,5,7,10] λ_D	[1,5] V
$1b : R_p = 0.5\lambda_D$	[1,5] V	1	[1,2,3,4,5,7,10] λ_D	[1,5] V
$2a : R_p = 0.1\lambda_D$	[1,5,10] V	[2,3,4,5,8,16]	10 λ_D	N/A
$2b : R_p = 0.5\lambda_D$	[1,5,10] V	[2,3,4,5,8,16]	10 λ_D	N/A

TABLE 1. Summary of parameters for two main numerical experiments.

boom to isolate the effects of having a guard radius that is different from that of the probe. We therefore vary R_g while keeping R_p fixed. We reuse the small and large probe with radius of $0.1\lambda_D$ and $0.5\lambda_D$, with probe and guard length of $L_p = L_g = 10\lambda_D$. In Buckingham's π theorem we can choose a dimensionless parameter for R_g, however one may find a better choice, where the two candidates are R_g/R_p, and R_g/λ_D. To investigate this we set $R_g/R_p = 2, 3, 4, 5, 8, 16$ for both the large and small probe. If R_g/R_p is a better parameter to consider, the curves should be quite similar. Although we cannot eliminate the parameter altogether, if the curves are similar, then the behaviour of the parameter in the function derived using Buckingham's π theorem gets simpler. In regression tasks in the future, this simplicity will likely mean that we can reduce the number of data points needed in the dimension of R_g/R_p or R_g/λ_D. We also run all configurations for three probe bias voltages of 1 V, 5 V and 10 V. The total number of simulations is 36 for this set-up, bringing the overall number of simulations for the whole project up to 92.

In the next section, we compare the currents from the present simulations with the Marholm–Marchand model (Marholm & Marchand 2020). To do this we first want to validate, and get an estimate of the error, for the currents in the present set-up with respect to the Marholm–Marchand model. The Langmuir library developed for the Marholm–Marchand model was constructed using a single cylinder (Marholm & Darian 2021). For that cylinder, the total current I is an integral of the profile function $i(z)$ which is the current as a function of length along the whole length of the probe. However, since the probe current $i(z)$ is a function of length for that cylindrical probe, defining the probe to be the part of the cylinder, for example, from 0 to $Z/2$ for a cylinder of length Z, the current I is readily available integrating over only the part of the probe from 0 to $Z/2$. This is effectively the same as splitting the cylinder into two separate simulated surfaces at $Z/2$, a probe and a guard in the simulator, and considering only the probe, defined as the surface starting at 0. These two will therefore give the same total current I. In order to verify that this is correct and to get an estimate of the errors for the large and small probe, we ran simulations with $R_g = R_p$, and $L_p = L_g = 10\lambda_D$. That means that in the simulations we define two cylinders of the same radius, and then compare with the Langmuir library, which is based on simulations of a single cylinder, where we set the probe length, and guard length equal to $10\lambda_D$ such that the library does an integration over only the $10\lambda_D$ that correspond to the probe. For the small probe $R_p = 0.1\lambda_D$ the relative errors in per cent with respect to FL, at the three chosen voltages are $[-3.52, -1.64, -0.08]$, and for the large probe $R_p = 0.5\lambda_D$ the relative errors in per cent are [6.64, 7.86, 9.45]. We see that the large probe has the largest error, and it is generally a positive change, meaning that we collect a larger current to the probe than predicted with the Langmuir model. We should keep these errors in mind when evaluating the results later on.

https://doi.org/10.1017/S0022377823001411 Published online by Cambridge University Press

3. Results

3.1. *Guard length*

The probe currents obtained in the first numerical experiment with set-up ID 1 from table 1 are shown in figure 2, with panel (*a*) including currents for the small probe (ID 1a), and panel (*b*) including currents for the large probe (ID 1b). The panels include both thermally charged boom (blue, yellow), and higher charged boom (green, red). The only parameter being varied here is L_g. It is reasonable to assume the current values to converge towards the current given by the FL theory. Convergence does not seem to have been exactly reached within the considered parameter space, although, it is in quantitative agreement and within 10 %. Similar to the FL theory, the probe needs to be $\gtrsim 10\lambda_D$ before the current $i(z)$ is close to the OML current at the probe center, but the probe needs to be $\gg 10\lambda_D$ before OML is a good approximation for the total current (Marholm & Marchand 2020). It does look like the currents will continue to converge towards the FL theory at some guard length longer than the $10\lambda_D$ chosen here, at least for the case of a small probe. The larger radius for the large probe might be large enough that it contributes to a small deviation from FL theory. The curves gather and flatten out in both cases around 6–$8\lambda_D$, we therefore deem this to be the length needed for a reasonable degree of convergence, and the length needed for the probes to have a small effect from the boom. For the boom to have zero effect on the probe, the guard needs to be longer than at least $10\lambda_D$, since the curves have not flattened out completely even at $10\lambda_D$. We also see that for the common usage of a guard of 2–$3\lambda_D$, the error from the charged boom will likely be significant. In addition, we can generally state that when the guard is short, the currents are significantly lowered due to the density depletion in the vicinity of the boom. This is therefore in agreement with previous assumptions that a long enough guard leads to minimal effect on currents. However, what is not in agreement is the scale length of the effect.

Another notable effect is that the currents are larger in some cases, with a visible peak at $L_g/\lambda_D = 3$ for the large probe with a thermal charging of the boom. A smaller local peak is seen at $L_g/\lambda_D = 4$ for the small probe. This shift in position suggests that this effect is at least dependent on R_p in addition to L_g. This is counterintuitive, as one would expect the boom to only reduce the currents to a certain degree as it has opposite polarity. This might be different for ion collection since then both boom and probe are normally negatively charged.

For the second experiment we have gathered all simulated currents in figure 3. While we compare results with the FL theory here, we should not expect the currents to coincide with the FL currents since the FL theory is applicable for the 'ideal' theory, where it is assumed that $R_g = R_p$. In this experiment the boom is removed from the simulations, and the only varying parameter is R_g. The simulation parameters are summarised in table 1 with set-up ID 2. In figure 3, panel (*a*) is again for the small probe, whereas panel (*b*) is for the large probe. The two panels do not follow the same trend, indicating that R_g/R_p is not the best choice of parameter for the dimensionless set of variables. However, we observe a peak for the currents in both panels. In dimensions of λ_D this is at $R_g = 0.8\lambda_D$ for the small probe, and $R_g = 1.5\lambda_D$ for the large probe. This is quite close considering the resolution of $0.5\lambda_D$ for the large probe. This, instead, suggests that R_g/λ_D is a better choice for dimensionless parameter to use. By using R_g/λ_D we also avoid issues in the mathematical model when assuming that $R_p \to 0$.

It is clear from figure 3, that the currents behave quite differently at high and low probe voltages. For a small probe, in panel (*a*) for the 1 V curve we observe a clear negative trend as the guard radius increases. This makes sense as a larger object collecting particles in the vicinity of the probe leaves fewer particles for the probe to collect. However, for both

https://doi.org/10.1017/S0022377823001411 Published online by Cambridge University Press

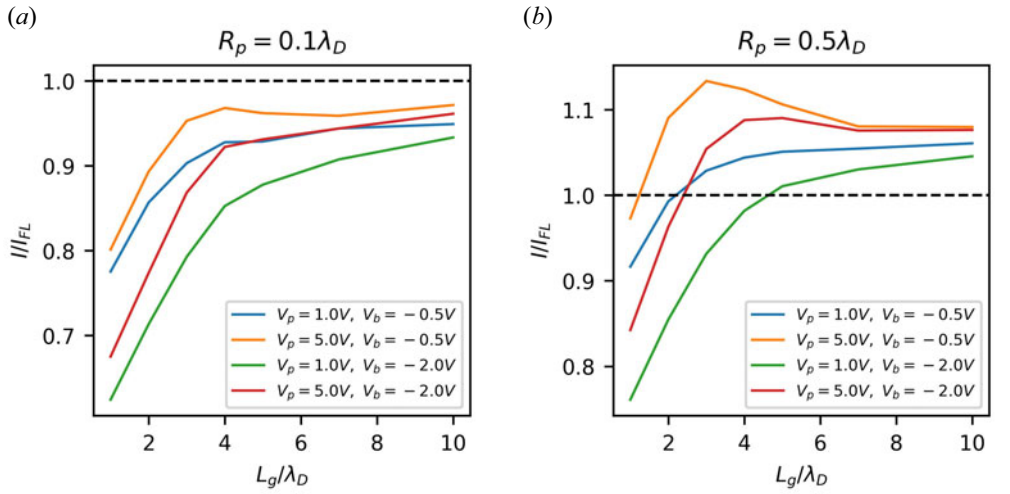

FIGURE 2. Normalised currents collected by the probe as a function of the guard length. The plots include one data point for each of the simulations listed in table 1 with the simulation ID 1. The guard length L_g is treated as a variable, and the four lines per panel correspond to the four possible configurations of the remaining parameters. The plot shows the ratio I/I_{FL}, where I is computed from the simulations, and I_{FL} is the current obtained from the FL model. Panel (*a*) contains data for the small probe with probe radius $R_p = 0.1\lambda_D$, and panel (*b*) contains data for the large probe with $R_p = 0.5\lambda_D$.

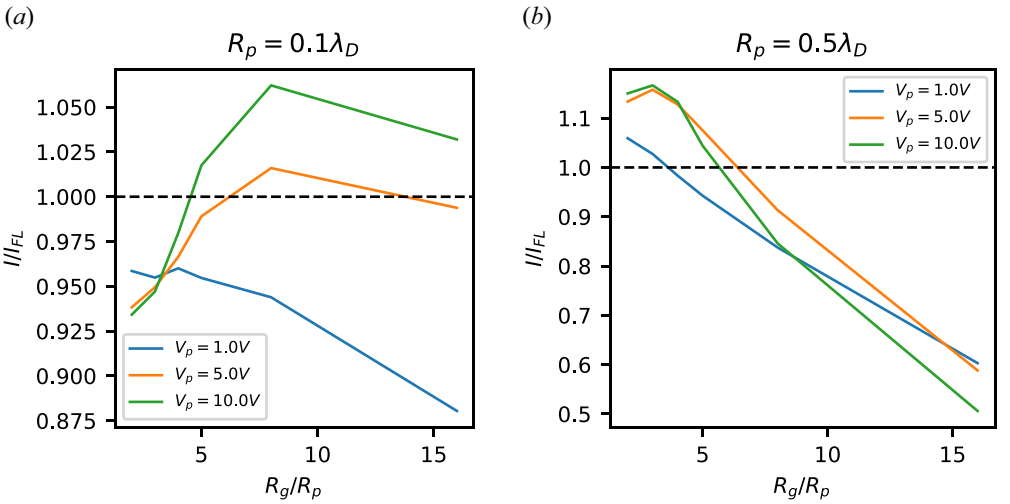

FIGURE 3. Normalised total currents as a function of the guard length for the second numerical experiment with the simulation ID 2 and parameters listed in table 1. The parameter R_g/R_p is treated as a variable, and the three lines in each panel correspond to the three probe biases simulated. The probe current is normalised I/I_{FL}, where I_{FL} is the current obtained from the FL theory. Panel (*a*) shows results for the small probe with probe radius $R_p = 0.1\lambda_D$, and panel (*b*) shows results for the large probe with $R_p = 0.5\lambda_D$.

https://doi.org/10.1017/S0022377823001411 Published online by Cambridge University Press

the 5 V and 10 V curves we see a peak in the curves, indicating that the guard increases the current to the probe at certain guard radii. This also seems to be true for the large probe, although it is less clear as there is only one simulated sample point before the peak. For the large probe the effect is quite significant when varying the ratio R_g/R_p. However, significant values for change in current to the probe of greater than 10 % occur for $R_g \gtrsim 4\lambda_D$.

3.2. *Guard radius*

The peaks in the currents seen in figure 3 can be further analysed by considering the currents as a function of position on the probe (i.e. $i = i(z)$), similarly to what has been done by Marholm & Marchand (2020). Similar to what we did in § 3.1, it would be ideal to compare the regression curves for $i(z)$ from the present simulations to the $i(z)$ curves obtained from the global regression in the FL theory, which are readily available in the Langmuir library (Marholm & Marchand 2020; Marholm & Darian 2021). However, since the changes in current observed in the present simulations are in some cases quite small, it might be misleading to make this comparison as it would be difficult to discern the source of the observed changes when the changes are smaller than the error with respect to the verification simulations. Therefore, we use the verification simulations as a comparison, and use the same local regression technique as in the FL library on the verification simulations and the simulations with ID 2 presented in table 1. The regression on the verification simulations are performed with the same method as the local regressions in the FL library, however, comparing regressions from verification simulations to R_g/R_p simulations will not include the small errors due to the global regression, assumptions on geometry, etc.

For this analysis, we selected 10-V-current curves from figure 3 and present the corresponding $i(z)$ regression curves in figure 4. The probe tip is set at $z = 0$, and the probe is attached to the guard at $z = 10\lambda_D$. The small probe $i(z)$ results are shown in panels (*a*,*c*), and the results for the large probe are shown in panels (*b*,*d*). The upper panels show the normalised current with respect to the OML current, $i(z)/i_{OML}(z)$. To differentiate between the effect of changing the guard radius and the finite length effects we also show in the lower panels the percentage error between $R_g = R_p$ curves and the $R_g \neq R_p$ curves as a function of z. In general, on the guard side the currents are lowered. This is followed by a relative current error increase towards the tip of the probe, although not at the tip, but at 2–4λ_D from the probe tip, and finally another drop in relative current error at the probe tip. The drop is with respect to the FL current, and is thus an increase with respect to the OML current, according to the FL library. Integrating over the $i(z)$ curves in figure 4 gives the total probe currents we see in figure 3. For small R_g, or lower values in figure 4(*a*,*c*) $R_g = 0.2$–$0.3R_p$, the peak in relative current is still lower than the comparison current $R_g = R_p$, in addition to the generally lower currents close to the guard. This means that an integral over this current will lead to a lowered current with respect to the FL current. For large $R_g = 0.8$–$1.6R_p$ this peak is large and wide, such that an integral over this curve will give a slightly larger current with respect to the FL current. For the intermediate values of R_g we see that there are indeed changes in the currents. However, the maxima and minima in the currents roughly cancel each other after integrating, leading to an overall negligible change in the total current to the probe. For large values of R_g, the larger values in 4(*b*,*d*), there is a more significant lowering of the current. However, this effect is along the whole probe, and it is most significant at the opposite end of the guard.

The aforementioned area of positive error in the $R_g = 1.5\lambda_D$ (yellow) curve in figure 4(*b*,*d*) is indeed interesting. In contrast to this area of the probe, the area closest to the guard, between the lower values of R_g in figure 4(*b*,*d*) to the larger values of R_g

https://doi.org/10.1017/S0022377823001411 Published online by Cambridge University Press

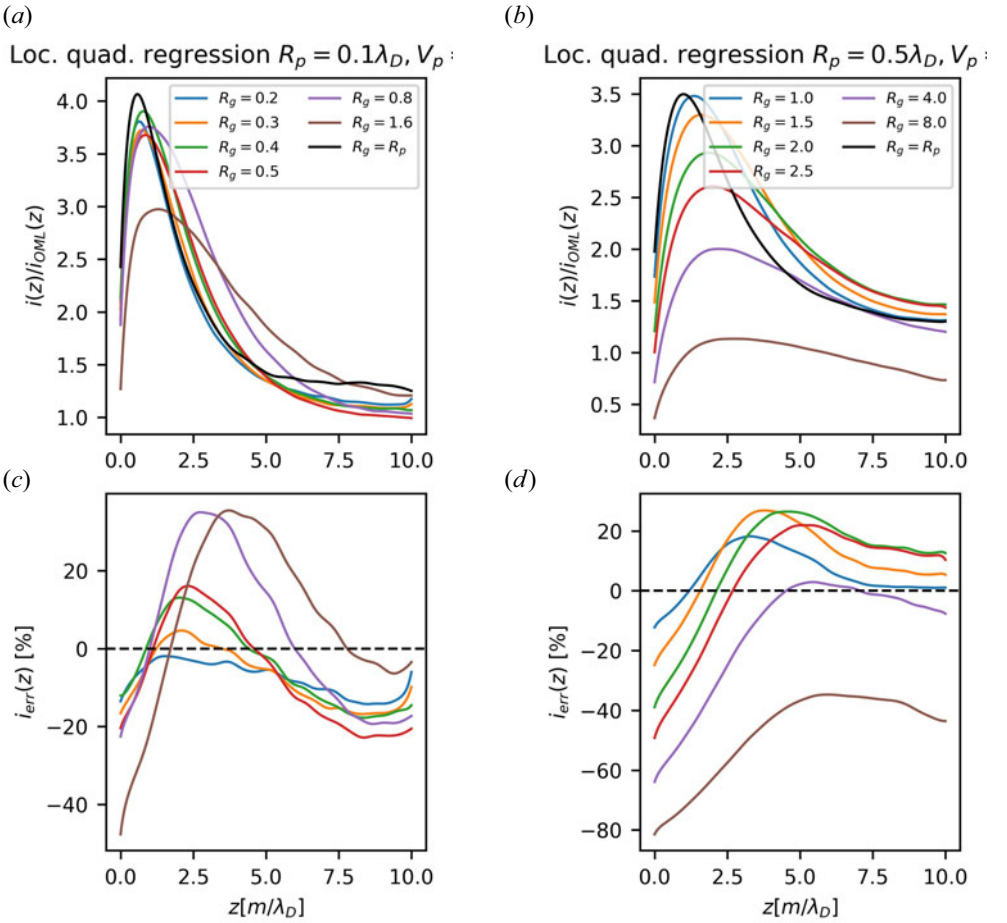

FIGURE 4. Normalised currents per unit length $i(z)$ as a function of position z along the probe for the second numerical experiment (*a*,*b*). There is one current curve shown for each simulated value of R_g. Values for the small probe $R_p = 0.1\lambda_D$ are to the left (*a*,*c*), and values for the large probe $R_p = 0.5$ are to the right (*b*,*d*). All legends in (*a*,*b*) are given in units of λ_D. Panels (*c*,*d*) show the percentage change i_{err} with respect to the $R_g = R_p$ curve (i.e. the FL current).

in figure 4(*a*,*c*) suggest that the guard's effect on the probe is opposite for the small and large guard in this range of parameters. The idea that the larger guard will serve as a sink of particles, leading to an overall lowering of the probe currents in its vicinity, is in opposition to this result. Therefore, other sheath effects must play an important role in this case.

3.3. *Guard radius effects on the sheath density*

To look closer at the effects of the guard on the probe currents, in figure 5 we plot slices of charge density and potential around the probe and guard from the same simulations as in figure 4(*a*,*c*), i.e. for the small probe biased at 10 V and for varying guard radius. The guard radius increases in each panel from $0.2\lambda_D$ (upper left panel) to $1.6\lambda_D$ (lower right panel), and each panel is split in two along the center of the probe in the z direction running the length of the probe. The left half shows the averaged charge density, and the right half

https://doi.org/10.1017/S0022377823001411 Published online by Cambridge University Press

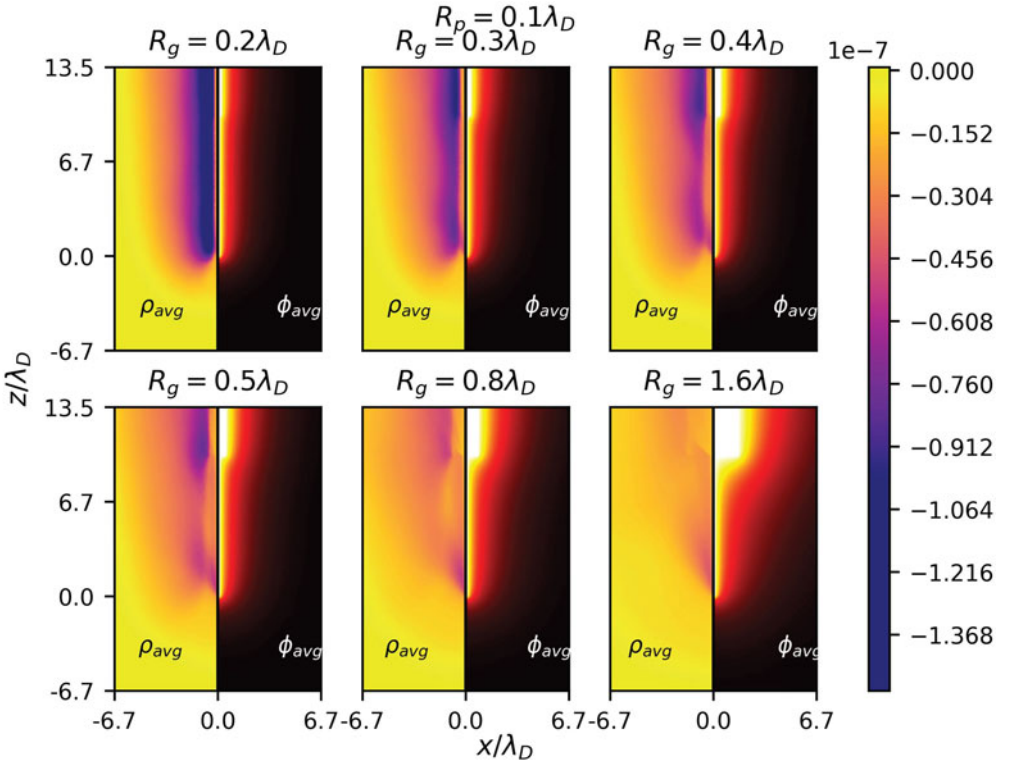

FIGURE 5. Slices in the normalised x–z directions of the average charge density ρ_{avg}, and average electric potential ϕ_{avg} in the vicinity of the probe and guard. The simulations selected are from the small probe $R_{\text{g}} = 0.1\lambda_{\text{D}}$ case. The colour bar refers to ρ_{avg} in units of C m^{-3}.

shows the averaged electric potential. The time-averaging follows the averaging scheme given by Marchand (2012) with the relaxation time of 1 μs. The added colour bar shows the colour map for the charge density. We omit the colour bar for the electric potential as this goes from 0 to 10 V since the probe is biased at 10 V.

Figure 5 shows the changes in the density sheath and electric potential as the guard radius is varied. For the charge density, an area of density depletion gets wider close to the probe with the width of the depletion area roughly equal to the guard radius. At transition, which in the present case is close to $R_{\text{g}} = 0.8\lambda_{\text{D}}$, the depletion area is overtaken by a density cone shape stemming from the tip of the probe. It is not clear currently if this cone shape is at the tip because the tip happened to be at $10\lambda_{\text{D}}$, or if it will always be at the tip of the probe. It does seem however that the peak in currents observed in figure 4 at 2–$4\lambda_{\text{D}}$ can be explained by the formation of this cone, as the peaks are located right on the inner edge of the cone structure. A possible explanation as to how the cone forms can be seen from taking into account the electric potential. In the fourth panel, for $R_{\text{g}} = 0.5\lambda_{\text{D}}$, it seems that particles travel from the edge of the guard towards the probe. Most of these particles are trapped in the potential well of the guard, and will follow the equipotential lines that are pointing slightly in the direction of the probe (radially inwards) in the area between 5–$10\lambda_{\text{D}}$ in this case. This gives a small number of particles the additional radial energy needed to overcome the trapping potential.

In figure 4(*a*,*c*) the smallest guard radius $R_{\text{g}} = 0.2\lambda_{\text{D}}$ has a slightly lower current along the whole probe, which might be explained by the density depletion gap close to the probe

https://doi.org/10.1017/S0022377823001411 Published online by Cambridge University Press

seen for the smaller values of R_g in figure 5. For these small values, the depletion leads to the lowering of the currents, and the funnelling effect discussed is not large enough to contribute to the current increase at any point.

4. Discussion

The currents in the upper panels of figure 4 include the FL end-effect resulting in an increased current, which is seen as a peak in the current towards the tip of the probe. The FL current peak is in this case 4 times larger (300 %) than the OML current. In present simulations, the largest change seen as a result of changing the guard radius is 40 % as long as $R_g < \lambda_D$, so the FL end-effect dominates in all the cases considered. However, since we only simulate probes with a probe length $L_p = 10\lambda_D$, and we see that there are changes in the current along the whole probe it is possible that there exists some configuration where the FL end-effect and the effect of varying R_g can contribute to the error on an equal scale. In addition, it seems likely that the cone shape observed at the probe tip appeared at the tip because the tip happens to be at $10\lambda_D$. The present set-up, where we assumed the probe length to have a minimal effect as long as the probe is sufficiently long for the change in the end-effects (including varying R_g) to be negligible, leaves room for further investigations and a follow-up study that includes a varying probe length in addition to the varying guard radius.

As mentioned earlier, it seems that R_g/λ_D is the best parameter to use for a model using the Buckingham's π theorem. However, the differences between the small probe and large probe do not seem to be negligible, and therefore R_p may also need to be included in the dimensionless set of variables when doing a regression. The initial assumption that R_p is small with respect to λ_D may no longer be valid for the $R_p = 0.5\lambda_D$ probe. This is supported by results in figure 3 where we see that (for relatively small guard radii) the currents for the small probe are all within a 5–7 % band, which is likely within the simulation error, whereas the errors for the large probe are >10 %. It is likely that $R_p = 0.5\lambda_D$ is the limit of this assumption, and for $R_p < 0.5\lambda_D$, R_p can be neglected, however, for $R_p \geqslant 0.5\lambda_D$, R_p should be included. In addition, evaluating the changes for a large R_g, if we take for example $R_g = 1.6\lambda_D$ (brown) curve from 4*a*,*c*), and $R_g = 1.5\lambda_D$ (yellow) curve from 4*b*,*d*), these two curves should be nearly equal if there were no dependence on R_p. For these curves we see a 20 % difference in the current errors at the tip of the probe. There is also an area of negative error for the small probe closer to the guard, while the large probe is positive in the same area. In addition, as seen in figure 3 when integrating over the two curves the difference is 10 % ($R_g/R_p = 16$ from panel (*a*) vs $R_g/R_p = 3$ from panel (*b*)). Therefore, the differences also seem to appear for higher values of R_g.

As a final example we could evaluate the applicability of these results to a real world scenario. We could for example consider the m-NLP system, which uses a probe with $R_p = 0.25$ mm (diameter of 0.5 mm) and $L_p = 25$ mm. For the guard the radius $R_g = 1$ mm (diameter of 2 mm), and guard length is $L_g = 15$ mm. We include also a quote on the m-NLP design by Hoang *et al.* (2018): 'The probes were designed to be much smaller than the Debye length of a few to tens of millimeter for common ionospheric plasma conditions'. With the Debye length of tens of millimetres the guard will be close to one Debye length or shorter. In the present numerical set-up the m-NLP probes will have a probe length of $3.6\lambda_D$, a guard length of $2.2\lambda_D$, and a guard radius of $\sim 0.1\lambda_D$. With these numbers we can see that the guard length will likely lead to significant errors. In addition, the design being for a few to tens of millimetres, and the usual assumption of $L_g = 1$–$2\lambda_D$ should not be considered sufficient. However, based on the limited present results, the small R_g and small difference in R_g/R_p likely do not contribute to a significant source of error.

https://doi.org/10.1017/S0022377823001411 Published online by Cambridge University Press

5. Conclusions

For the first numerical experiment, where we considered a varying guard length and included a boom, we can summarise the results as follows. In order for the boom to have a small effect on the probe current, the guard needs to be 6–8λ_D long. For a zero effect, the guard needs to be longer (or much longer) than 10λ_D. As mentioned earlier, to include the parameter L_g/λ_D in an empirical model we will need up to 1000 simulations. This is not impossible, but expensive computationally considering that the problem can be mostly avoided by enforcing the requirement on the guard length of 6–8λ_D long. However, it may be important in a study where new data are compared with older data if these data were taken with a probe design where only a guard length of 2λ_D was used as the requirement for the shortest λ_D in its operating range.

For the second numerical experiment, a zero effect on the total current to the probe is only possible for $R_p = R_g$, and this is often practically impossible. However, the effect is small enough that it should not be the major source of error. Again, including R_g as a parameter in an empirical model is possible, but computationally expensive. We therefore need justification for this to be necessary. However, this justification may not be strong as R_g usually has a small effect on the total probe current. However, this is only true as long as the guard radius is not too large with respect to the Debye length. This is usually the case for most of the needle Langmuir probes, however, it is a good practice to explicitly check this condition when using data from a particular probe system.

Acknowledgements

This research is a part of the 4DSpace Strategic Research Initiative at the University of Oslo. R.M. thanks the Natural Sciences and Engineering Research Council of Canada for its financial support. S.M.B. is grateful towards IFE and Øyvind Jensen for permission to participate in this project.

Editor Edward Thomas, Jr. thanks the referees for their advice in evaluating this article.

Funding

This work received funding from the European Research Council (ERC) under the European Union's Horizon 2020 research and innovation programme (Grant Agreement No. 866357, POLAR-4DSpace). This study was also supported in part by the Research Council of Norway Grant 275653.

Declaration of interests

The authors report no conflict of interest.

Data availability

All simulations presented can be reproduced using PTetra v50h. Copies of PTetra can be obtained upon request from Richard Marchand. The simulation data that support the findings of this study are openly available in Zenodo at http://doi.org/10.5281/zenodo.8182838.

REFERENCES

ANDERSON, P.C. 2012 Characteristics of spacecraft charging in low Earth orbit. *J. Geophys. Res.* **117**, A7.

ANDERSON, P.C., HANSON, W.B., COLEY, W.R. & HOEGY, W.R. 1994 Spacecraft potential effects on the Dynamics Explorer 2 satellite. *J. Geophys. Res.* **99** (A3), 3985–3997.

https://doi.org/10.1017/S0022377823001411 Published online by Cambridge University Press

Bekkeng, T., Barjatya, A., Hoppe, U.-P., Pedersen, A., Moen, J., Friedrich, M. & Rapp, M. 2013 Payload charging events in the mesosphere and their impact on Langmuir type electric probes. *Ann. Geophys*. **31**, 187–196.

Bekkeng, T.A., Jacobsen, K.S., Bekkeng, J.K., Pedersen, A., Lindem, T., Lebreton, J.-P. & Moen, J.I. 2010 Design of a multi-needle Langmuir probe system. *Meas. Sci. Technol*. **21** (8), 085903.

Buchert, S.C., Eriksson, A., Gill, R., Nilsson, T., Åhlen, L., Wahlund, J.-E., Knudsen, D., Burchill, J., Archer, W., Kouznetsov, A., *et al.* 2014 First results from the Langmuir Probes on the Swarm satellites. In *2014 XXXIth URSI General Assembly and Scientific Symposium (URSI GASS)*, pp. 1–1. IEEE.

Buckingham, E. 1914 On physically similar systems; illustrations of the use of dimensional equations. *Phys. Rev*. **4** (4), 345–376.

Eriksson, A.I. & Wahlund, J.-E. 2006 Charging of the Freja Satellite in the Auroral Zone. *IEEE Trans. Plasma Sci*. **34** (5), 2038–2045.

Eriksson, A.I., Boström, R., Gill, R., Åhlén, L., Jansson, S.-E., Wahlund, J.-E., André, M., Mälkki, A., Holtet, J.A., Lybekk, B., *et al.* 2007 RPC-LAP: the Rosetta Langmuir Probe Instrument. *Space Sci. Rev*. **128** (1), 729–744.

Garrett, H.B. 1981 The charging of spacecraft surfaces. *Rev. Geophys*. **19** (4), 577–616.

Gussenhoven, M.S., Hardy, D.A., Rich, F., Burke, W.J. & Yeh, H.-C. 1985 High-level spacecraft charging in the low-altitude polar auroral environment. *J. Geophys. Res*. **90** (A11), 11009–11023.

Gustafsson, G., Boström, R., Holback, B., Holmgren, G., Lundgren, A., Stasiewicz, K., Åhlén, L., Mozer, F.S., Pankow, D., Harvey, P., *et al.* 1997 The electric field and wave experiment for the cluster mission. *Space Sci. Rev*. **79** (1), 137–156.

Hoang, H., Clausen, L.B.N., Røed, K., Bekkeng, T.A., Trondsen, E., Lybekk, B., Strøm, H., Bang-Hauge, D.M., Pedersen, A., Spicher, A., *et al.* 2018 The Multi-Needle Langmuir Probe System on Board NorSat-1. *Space Sci. Rev*. **214** (4), 75.

Holback, B., Jansson, S.E., Åhlén, L., Lundgren, G., Lyngdal, L., Powell, S. & Meyer, A. 1994 The Freja wave and plasma density experiment. *Space Sci. Rev*. **70** (3), 577–592.

Jacobsen, K.S., Pedersen, A., Moen, J.I. & Bekkeng, T.A. 2010 A new Langmuir probe concept for rapid sampling of space plasma electron density. *Meas. Sci. Technol*. **21** (8), 085902.

Laframboise, J.G. 1966 Theory of spherical and cylindrical langmuir probes in a collisionless, Maxwellian plasma at rest. PhD thesis, University of Toronto.

Liu, G., Marholm, S., Eklund, A.J., Clausen, L. & Marchand, R. 2023 m-NLP inference models using simulation and regression techniques. *J. Geophys. Res*. **128** (2), e2022JA030835.

Marchand, R. 2012 PTetra, a tool to simulate low orbit satellite–plasma interaction. *IEEE Trans. Plasma Sci*. **40** (2), 217–229.

Marchand, R. & Resendiz Lira, P.A. 2017 Kinetic simulation of spacecraft–environment interaction. *IEEE Trans. Plasma Sci*. **45** (4), 535–554.

Marholm, S. 2019 localreg: local polynomial regression. https://github.com/sigvaldm/localreg.git.

Marholm, S. & Darian, D. 2021 langmuirproject/langmuir:. https://zenodo.org/record/5469073.

Marholm, S. & Marchand, R. 2019 99 Probes. https://zenodo.org/record/3269686.

Marholm, S. & Marchand, R. 2020 Finite-length effects on cylindrical Langmuir probes. *Phys. Rev. Res*. **2** (2), 023016.

Mott-Smith, H.M. & Langmuir, I. 1926 The theory of collectors in gaseous discharges. *Phys. Rev*. **28** (4), 727–763.

Olowookere, A. & Marchand, R. 2021 Fixed bias probe measurement of a satellite floating potential. *IEEE Trans. Plasma Sci*. **PP**, 1–9.

Whipple, E.C. 1981 Potentials of surfaces in space. *Rep. Prog. Phys*. **44** (11), 1197–1250.

Yeh, H.C. & Gussenhoven, M.S. 1987 The statistical electron environment for Defense Meteorological Satellite Program Eclipse charging. *J. Geophys. Res*. **92** (A7), 7705–7715.

https://doi.org/10.1017/S0022377823001411 Published online by Cambridge University Press